

# Localized Photoreceptor Ablation Using Femtosecond Pulses Focused With Adaptive Optics

Kamal R. Dhakal<sup>1</sup>, Sarah Walters<sup>1,2</sup>, Juliette E. McGregor<sup>1</sup>, Christina Schwarz<sup>1,3</sup>, Jennifer M. Strazzeri<sup>4</sup>, Ebrahim Aboulizadeh<sup>1</sup>, Brittany Bateman<sup>4</sup>, Krystel R. Huxlin<sup>1,2,4</sup>, Jennifer J. Hunter<sup>1,2,4</sup>, David R. Williams<sup>1,2</sup>, and William H. Merigan<sup>1,4</sup>

<sup>1</sup> Center for Visual Science, University of Rochester, Rochester, NY, USA

<sup>2</sup> The Institute of Optics, University of Rochester, Rochester, NY, USA

<sup>3</sup> Institute for Ophthalmic Research, University of Tübingen, Tübingen, Germany

<sup>4</sup> Flaum Eye Institute, University of Rochester, Rochester, NY, USA

**Correspondence:** Kamal R. Dhakal, Center for Visual Science, University of Rochester, 601 Elmwood Avenue, Box 319, Rochester, NY 14642, USA. e-mail: [dhakalrkamal@gmail.com](mailto:dhakalrkamal@gmail.com)

**Received:** August 14, 2019

**Accepted:** April 9, 2020

**Published:** June 16, 2020

**Keywords:** adaptive optics; femtosecond laser; retinal degeneration; vision restoration; retinal imaging

**Citation:** Dhakal KR, Walters S, McGregor JE, Schwarz C, Strazzeri JM, Aboulizadeh E, Bateman B, Huxlin KR, Hunter JJ, Williams DR, Merigan WH. Localized photoreceptor ablation using femtosecond pulses focused with adaptive optics. *Trans Vis Sci Tech.* 2020;9(7):16, <https://doi.org/10.1167/tvst.9.7.16>

**Purpose:** The development of new approaches to human vision restoration could be greatly accelerated with the use of nonhuman primate models; however, there is a paucity of primate models of outer retina degeneration with good spatial localization. To limit ablation to the photoreceptors, we developed a new approach that uses a near-infrared ultrafast laser, focused using adaptive optics, to concentrate light in a small focal volume within the retina.

**Methods:** In the eyes of eight anesthetized macaques, 187 locations were exposed to laser powers from 50 to 210 mW. Laser exposure locations were monitored for up to 18 months using fluorescein angiography (FA), optical coherence tomography (OCT), scanning laser ophthalmoscopy (SLO), adaptive optics scanning laser ophthalmoscope (AOSLO) reflectance imaging, two-photon excited fluorescence (TPEF) ophthalmoscopy, histology, and calcium responses of retinal ganglion cells.

**Results:** This method produced localized photoreceptor loss with minimal axial spread of damage to other retinal layers, verified by *in-vivo* structural imaging and histologic examination, although in some cases evidence of altered autofluorescence was found in the adjacent retinal pigment epithelium (RPE). Functional assessment using blood flow imaging of the retinal plexus and calcium imaging of the response of ganglion cells above the photoreceptor loss shows that inner retinal circuitry was preserved.

**Conclusions:** Although different from a genetic model of retinal degeneration, this model of localized photoreceptor loss may provide a useful testbed for vision restoration studies in nonhuman primates.

**Translational Relevance:** With this model, a variety of vision restoration methods can be tested in the non-human primate.

## Introduction

Although several strategies for vision restoration<sup>1–6</sup> show promise for use in humans blinded by retinal disease, they are largely based on the use of the rodent retinal degeneration model, which is not ideal for predicting translational efficacy. Nonhuman primates are an especially valuable model for preclinical vision restoration studies because their visual system is closest

to that of humans, with a similar distribution of rods and cones,<sup>7</sup> a specialized fovea,<sup>8</sup> and almost identical retinocortical architecture. Furthermore, perceptual capabilities such as contrast sensitivity, visual acuity and motion direction discrimination are comparable in macaque and human.<sup>9</sup> Unfortunately, nonhuman primate models of photoreceptor loss are still at an early stage of development.

Given the challenges of working with naturally occurring eye disease models in macaque<sup>10</sup> other

**Table 1.** Summary of Nonhuman Primates Used in the Study

Macaque ID	Species	Age (y)	Sex	Eye	Axial Length (mm)
M1	Fascicularis	6	M	OD/OS	17.20/17.10
M2	Fascicularis	6	M	OD	17.87
M3	Fascicularis	5	F	OS	17.15
M4	Fascicularis	5	F	OD/OS	17.10/17.14
M5	Fascicularis	6	F	OD/OS	17.92/17.75
M6	Fascicularis	6	F	OD/OS	17.88/17.87
M7	Mulatta	19	M	OS	20.52
M8	Fascicularis	8	M	OD/OS	17.55/17.56

approaches have been developed, including toxicant exposure<sup>11–13</sup> and intense continuous-wave (CW) laser light to induce photoreceptor degeneration.<sup>14</sup> These methods have proven inadequate for studying isolated photoreceptor damage as all methods used to date appear to damage other retinal neurons and may produce substantial scarring.<sup>14</sup> Furthermore, CW exposure produces cell loss with poor spatial and axial localization and may cause collateral damage due to dissipation of heat to the surrounding tissue.<sup>15</sup> On the other hand, it is challenging to achieve permanent photoreceptor loss using subthreshold laser power.<sup>16</sup>

Here, we report an improved method for photoreceptor ablation in macaque. Building on the extensive literature of laser-retina interactions,<sup>15,17–22</sup> we sought to limit the axial spread of damage by using adaptive optics to focus a femtosecond laser at the photoreceptor layer. Previous studies have used *in-vivo* imaging to examine photoreceptor loss in humans.<sup>23</sup> In this study we used optical coherence tomography (OCT) and adaptive optics scanning laser ophthalmoscope (AOSLO) imaging of retinal structure and function over a period of up to 18 months after damage to identify laser parameters that give complete photoreceptor loss that is laterally and axially confined and confirmed this by retinal histology.

## Methods

### Animal Preparation

Eight monkeys (Table 1) were pair-housed in a vivarium accredited by the Assessment and Accreditation of Laboratory Animal Care committee and subjects were handled as per the protocols prescribed and approved by the University of Rochester's committee for animal research and in accordance with the Association for Research in Vision and Ophthalmology (ARVO) Animal Statement for the Use of Animals in Ophthalmic and Vision Research. This study was

conducted in strict agreement with the recommendations in the Guide for the Care and Use of Laboratory Animals of the National Institutes of Health.

Before each imaging session, the monkeys were anesthetized with a mixture of ketamine (5–20 mg/kg), midazolam (0.25mg/kg), and glycopyrrolate (0.017 mg/kg) given intramuscularly and maintained with inspired isoflurane (1.5–3%). Rocuronium bromide (20–55 µg/kg/hour) was given for paralysis and the animal was artificially respired. Body temperature was maintained at 37.8°C to 38.9°C using a heated airflow system and warming packs. Vital signs were monitored constantly and recorded every 15 minutes throughout the imaging session using electrocardiography. Lactated Ringer's solution with 5% dextrose was given by intravenous drip for fluid replenishment. Pupil dilation and cycloplegia were induced with up to four drops each of phenylephrine hydrochloride (2.5%) and tropicamide (1%). If the pupil failed to dilate, up to four drops of cyclopentolate hydrochloride (1%) solution were administered. A lid speculum was used to keep the eye open. To prevent dehydration of the cornea and mitigate refractive error, a contact lens lubricated with Genteal (Alcon, Fort Worth, TX, USA) was placed on the eye. A motorized stereotaxic cart consisting of a three-axis translation stage combined with a two-axis goniometer was used to move the animal's pupil in three dimensions so as to align with the exit pupil of the imaging system and navigate along blood vessels to the retinal location to be imaged by moving the animal. At the end of the imaging session, anesthesia was reversed with neostigmine (0.05 mg/kg) and glycopyrrolate (0.01 mg/kg) given intravenously. Imaging sessions lasted up to six hours and were repeated no more than once per week.

### Ultrafast Laser Exposures

A two-photon adaptive optics scanning light ophthalmoscope (2P-AOSLO) described in the follow-

ing section was used to deliver ultrafast laser exposures. To induce selective damage to photoreceptors, the Ti:Sapphire femtosecond laser was focused at the outer nuclear layer (ONL). A total of 187 retinal locations, ranging in field sizes from  $0.79^\circ \times 0.87^\circ$  to  $1.19^\circ \times 1.39^\circ$ , were exposed to an average laser power ranging from 50 to 210 mW and for durations ranging from 106 to 335 ms. A computer-controlled shutter (SH1; Thorlabs Inc., Newton, NJ, USA) restricted exposure duration. The field size was determined by computer-controlled scanners, which operated at a frame rate of 26.5 Hz. Exposed locations were monitored for up to 18 months after exposure using OCT, scanning laser ophthalmoscopy (SLO), and AOSLO reflectance and two-photon excited fluorescence (TPEF) imaging modalities.

## 2P-AOSLO

An AOSLO designed for TPEF imaging of the primate retina, which has been described elsewhere,<sup>24</sup> was used for both reflectance and TPEF imaging of the retina. AOSLO imaging of reflected light, using both confocal and nonconfocal detection methods, was performed before and after the laser exposure to assess the loss of photoreceptors, as well as any effects on the vasculature. TPEF imaging was conducted after the laser exposure for functional measurement of the visual cycle in photoreceptors as described elsewhere.<sup>24,25</sup> Briefly, a Ti:Sapphire femtosecond laser (55 fs, 80 MHz, 730 nm, Mai Tai XF-1 with DeepSee attachment; Spectra-Physics, Santa Clara, CA, USA), compensated for second-order dispersion arising from both the optics of the AOSLO and the eye, was used to excite TPEF; the maximum power at the cornea was 3.5 to 4.5 mW. An 840-nm superluminescent diode was used for wavefront sensing with a Shack-Hartmann wavefront sensor, and a maximum power of 45  $\mu$ W was incident on the cornea. A deformable mirror corrected aberrations and was used to focus the light in different retinal layers. A 790-nm laser diode was used for reflectance imaging. All sources were cofocused at the retina. The focal spot was raster scanned across the retina with a resonant and a piezo scanner. All images captured were with a  $2^\circ \times 2.2^\circ$  field of view ( $X = 436$  pixels and  $Y = 480$  pixels) at a frame rate of 26.5 Hz. Two photomultiplier tubes (PMTs) captured reflected light from the 790 nm and 730 nm sources in confocal reflectance configuration. Additionally, the 730-nm reflectance channel was used for nonconfocal multi-offset imaging, which has been described elsewhere.<sup>25</sup> A third PMT for TPEF imaging (excitation: 730 nm; detection: 400–550 nm) was used. The TPEF time course data was adapted using a method described

elsewhere<sup>26</sup> with an exponential function  $y = \Delta F/F e^{-t/\tau} + 1$ , where  $\tau$  is the time constant of TPEF increase and  $\Delta F/F$  is the relative increase in TPEF.

## RPE Autofluorescence Imaging

Methods for *in-vivo* AOSLO autofluorescence imaging of individual RPE cells in macaques are described elsewhere.<sup>27</sup> This was performed using a single photon AOSLO system described elsewhere.<sup>28</sup> Briefly, we captured two channels of AOSLO images simultaneously: a confocal reflectance image of the photoreceptor cone mosaic using a 790-nm superluminescent diode and a fluorescence image to detect RPE autofluorescence. The RPE lipofuscin autofluorescence excitation wavelength was 561 nm and emission was detected over a wavelength range of 40 nm centered at 624 nm. An additional channel (840-nm light) was used for measuring wavefront aberrations. During imaging, the eye's aberrations were measured in real time by a Hartmann-Shack wavefront sensor and were corrected using a deformable mirror that was placed in the path conjugate to the entrance pupil. The intensities of the imaging lights at the macaque pupil were 20 to 40  $\mu$ W (561 nm), 250  $\mu$ W (790 nm), and 30 to 40  $\mu$ W (840 nm).

## Confocal SLO and OCT Imaging

Femtosecond laser damage was assessed with multiple clinical and laboratory imaging modalities. The retina was imaged before and after every session of femtosecond laser exposure using a confocal SLO (HRA + OCT; Heidelberg Engineering, Heidelberg, Germany) using a  $30^\circ$  field of view (1536 pixels). Imaging was performed in each of the following modalities: blue-light reflectance (488 nm), blue-light autofluorescence (Ex: 488 nm, Em: 510 nm), infrared reflectance (815 nm), and infrared autofluorescence (Ex: 786 nm, Em: 810–840 nm). Fourier-domain OCT scans of exposed locations were captured with an axial resolution of 3.9  $\mu$ m using the same instrument. During this period, confocal SLO images and OCT scans were visually inspected for qualitative changes in reflectivity or autofluorescence intensity.

## FA

The time course of choroidal leakage of fluorescein was tracked for six lesions made at various powers on the same day (Monkey M1). FA was obtained with a confocal SLO (Spectralis HRA + OCT, Heidelberg, Germany) using a field size of  $30^\circ$ , (1536 pixels) at

1 hour, 48 hours, and 72 hours after exposures. For each measure, 7.7 mg/kg of sodium fluorescein was injected intravenously, and FA images were taken over the next six minutes. FA images were screened for potential choroidal leakage.

## Calcium Imaging

Calcium imaging using GCaMP6s was used to assess whether the laser exposure of the photoreceptors compromised the response of the overlying ganglion cells in monkey M3. This was performed near the fovea of monkey M3 using the AOSLO system as described elsewhere.<sup>28</sup> A localized scotoma was created by ablating photoreceptors directly under the ganglion cell layer using the ultrafast laser (average power 150 mW, duration 106 ms, and  $0.79^\circ \times 0.87^\circ$  field of view). Foveal retinal ganglion cells (RGCs) are laterally displaced from the central foveal photoreceptors they serve, forming a ring at the margin of the foveal pit. This means that in contrast to other species and other retinal locations, it is possible to expose these ganglion cells to the lesioning light, ablating the photoreceptors directly beneath, without compromising the laterally displaced photoreceptor input to these RGCs. Thus the unique topography of the fovea makes it possible to directly assess the functional impact on RGCs lying directly above the damaged photoreceptors.

To achieve GCaMP6s expression in the foveal ganglion cells, the animal was injected intravitreally with 100  $\mu\text{L}$  of AAV2-CAG-GCaMP6s with a titer of  $1.94 \times 10^{13}$  viral genomes per milliliter. Expression was monitored using the blue autofluorescence modality of a confocal SLO (Heidelberg Spectralis). A 488 nm, 4.9  $\text{mW}/\text{cm}^{-2}$  laser source was focused on the ganglion cell layer to excite GCaMP6s fluorescence that was detected in a 520/35 nm emission band. A pinhole of eight Airy disc diameters was used to maximize signal collection. A panretinal 590 nm LED 0.8  $\text{mW}/\text{cm}^{-2}$  flicker stimulus was presented at 0.2 Hz for 90 seconds to drive retinal activity while GCaMP6s fluorescence was recorded. Confocal reflectance images of the photoreceptor layer were recorded simultaneously for image registration.

## Histologic Preparation

Monkeys designated for retinal histologic examination (M2 and M4) were euthanized and underwent perfusion with 2.5% glutaraldehyde + 4% paraformaldehyde in 0.1 mol/L phosphate buffer as described previously.<sup>23</sup> Briefly, after perfusion, the eyes were dissected, the anterior chambers were removed, and the posterior globes were immersion-fixed

overnight in 2.5% glutaraldehyde + 4% paraformaldehyde in 0.1 mol/L phosphate buffer at 4°C. The optic nerve, foveal regions, and regions containing the laser lesions were dissected from the globes. They were placed in 0.1 mol/L phosphate buffer overnight, rinsed five times with the same buffer over a total of one hour before dehydration with graded concentrations of ethanol (50%, 70%, 80%, 95%, and 100%, two changes each) also over a total of one hour. The tissue was then defatted using acetone before infiltration with glycol methacrylate plastic (Technovit H7100, no. 14653; Electron Microscopy Sciences, Hatfield, PA, USA) and embedding in molds (no. 70176-30; Electron Microscopy Sciences) at room temperature. Sections 3  $\mu\text{m}$  thick were cut through regions of interest using a rotary microtome (MICROM HM355S International, Walldorf, Germany), affixed to glass slides, and stained with Multiple Stain Solution (no. 08824; Polysciences, Inc., Warrington, PA, USA) before imaging with a light microscope in brightfield mode (BX53; Olympus, Tokyo, Japan).

## Vasculature Imaging

Vasculature imaging to assess the integrity of deep and superficial blood vasculature of the retina was performed using 790-nm reflectance channel in the 2P-AOSLO system described in the prior section. This study did not quantify measures of blood flow that can only be done by taking high-speed line scan images of single locations along blood vessels. A through focus movie was created from the images captured at frame rate 26.5 Hz while manually changing the AOSLO focal plane through photoreceptors to ganglion cell layer, and movies at fixed depths (superficial and deep) are shown in Supplementary Movies S1 and S2. Image J was used to create motion contrast images by taking the standard deviation of stacked time series images.

## Data Analysis

During AOSLO imaging, the high signal-to-noise ratio (SNR) reflectance videos and low SNR TPEF videos were recorded simultaneously with the pulsed 730 nm laser. Dual-image registration software<sup>29</sup> computed the eye motion from the high-SNR videos and coregistered both the high and the low-SNR video. The same strategy of coregistration was used for RPE imaging.

To quantify the axial extent of damage as a function of average power, measurements were made on OCT B-scans through the center of each exposure. ImageJ software was used to draw a line segment axially across

**Table 2.** Summary of Exposures

Macaque	Average Power (mW)	Exposure (ms)	Exposed Area	Imaging Modality			Remarks
				OCT	AOSLO	HRA	
M1	210 ± 2	335	1.19° × 1.39°	2\2	2\2	2\2	<sup>a</sup>
M1	210 ± 2	259	1.19° × 1.39°	2\2	2\2	2\2	<sup>b</sup>
M1	210 ± 2	183	0.79° × 0.87°	2\2	2\2	2\2	<sup>b</sup>
M1	210 ± 2	183	1.19° × 1.39°	2\2	2\2	2\2	
M1	210 ± 2	106	0.79° × 0.87°	3\3	3\3	3\3	
M1	210 ± 2	106	1.19° × 1.39°	2\2	2\2	2\2	
M1, M3	180 ± 2	106	0.79° × 0.87°	4\4	4\4	4\4	
M1, M2, M3	150 ± 2	106	0.79° × 0.87°	4\4	4\4	4\4	
M1, M7	130 ± 2	106	0.79° × 0.87°	3\3	3\3	3\3	
M1, M3, M4, M6	120 ± 2	106	0.79° × 0.87°	14\14	14\14	14\14	
M4, M5, M6, M8	110 ± 2	106	0.79° × 0.87°	42\42	42\42	42\42	
M1, M4, M5, M6, M7, M8	100 ± 2	106	0.79° × 0.87°	50\50	50\50	50\50	
M1, M3, M4, M5, M7, M8	90 ± 2	106	0.79° × 0.87°	54\54	54\54	54\54	
M1	80 ± 2	106	0.79° × 0.87°	1\1	1\1	1\1	
M1	68 ± 2	106	0.79° × 0.87°	0\1	0\1	1\1	
M1	50 ± 2	106	0.79° × 0.87°	0\1	0\1	0\1	

<sup>a</sup>Severe damage and vasculature rupture observed.

<sup>b</sup>Collateral damage observed.

the lesion, and the line segment length was plotted as a function of laser power.

For calcium imaging data, analysis was performed by Fourier transforming the time-course profile of GCaMP6s fluorescence. Two spatial segmentation masks for individual retinal ganglion cells were created, one containing cells within the boundary of the exposure as identified on confocal reflectance image of the photoreceptor layer, and a second containing cells superior to the exposure in the same frame. These masks were applied to the frame-registered videos. The fluorescence time course for each cell was Fourier-transformed to extract the amplitude of the response at the visual stimulus frequency. Average Fourier transforms for all cells inside and all cells outside of the exposed area were created to assess the impact of laser exposure.

(90–120 mW). Approximately 100 mW intensity was required to reliably damage all photoreceptors, something that was subsequently confirmed by histology (see Fig. 4). Figure 1 shows examples of the AOSLO appearance of the retina after exposures to three laser intensities (50, 150, and 210 mW). The left column shows reflectance images focused at the level of photoreceptors, illustrating a high level of structural detail visible due to the waveguiding of the photoreceptor outer segments. No change in waveguiding of photoreceptor is seen for the lowest intensity laser exposure in Figure 1a. The structural detail is greatly reduced within the exposed regions, as is visible at the center of Figures 1b and 1c. The right column of Figures 1d to 1f shows multi-offset aperture images of the same region, which reveals visible inner segments across the entire field of view except within the laser exposed regions at the two laser intensities as shown in Figures 1e and 1f.

## Results

### Effect on Photoreceptors

#### *In-Vivo* Structural Assessment of Photoreceptors

Table 2 summarizes the parameters of all laser exposures used in this study and visible changes observed in exposed locations using different imaging modalities. The vast majority of laser exposures were at the intermediate levels of laser intensity

#### *In-Vivo* Functional Measurement of Photoreceptors

We tested function of the visual cycle in exposed regions by collecting the time course of TPEF from the photoreceptors using approaches described elsewhere.<sup>25,26</sup> The left column shows the two-photon fluorescence image following exposure to a lower intensity 50 mW (Fig. 2a) and a moderate laser intensity at 130 mW (Fig. 2c). The time course

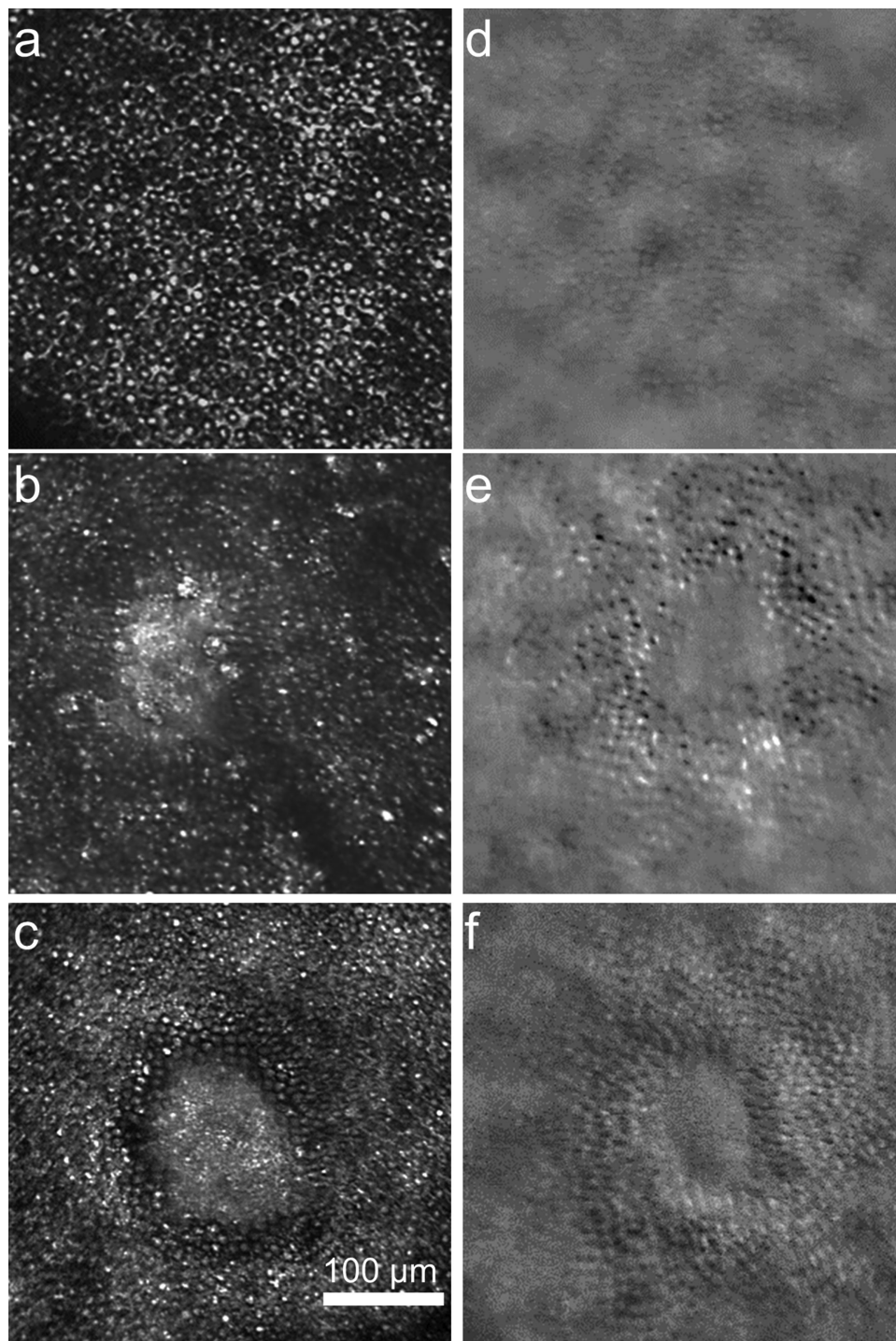


**Figure 1.** AOSLO images of photoreceptors post-lesion. *Left panels* show 730-nm reflectance images after 50 mW (a), 150 mW (b), and 210 mW (c) exposures of 106 ms with corresponding multi-offset aperture images to the right (d–f) (monkey M1).

of TPEF from within and surrounding the exposed area is plotted in [Figures 2b](#) and [2d](#). Photoreceptors at the location of the lower intensity laser exposure (50 mW, 106 ms) did not show any noticeable changes in either structure or function as shown in [Figures 2a](#) and [2b](#), whereas photorecep-

tors had substantially less TPEF at the location of higher laser exposure (210 mW, 106 ms) as seen in [Figure 2d](#), suggesting a dysfunctional visual cycle, whereas the photoreceptors outside the exposed region appeared normal. We found a similar result at all other power levels except at 50 mW. [Table 3](#) shows

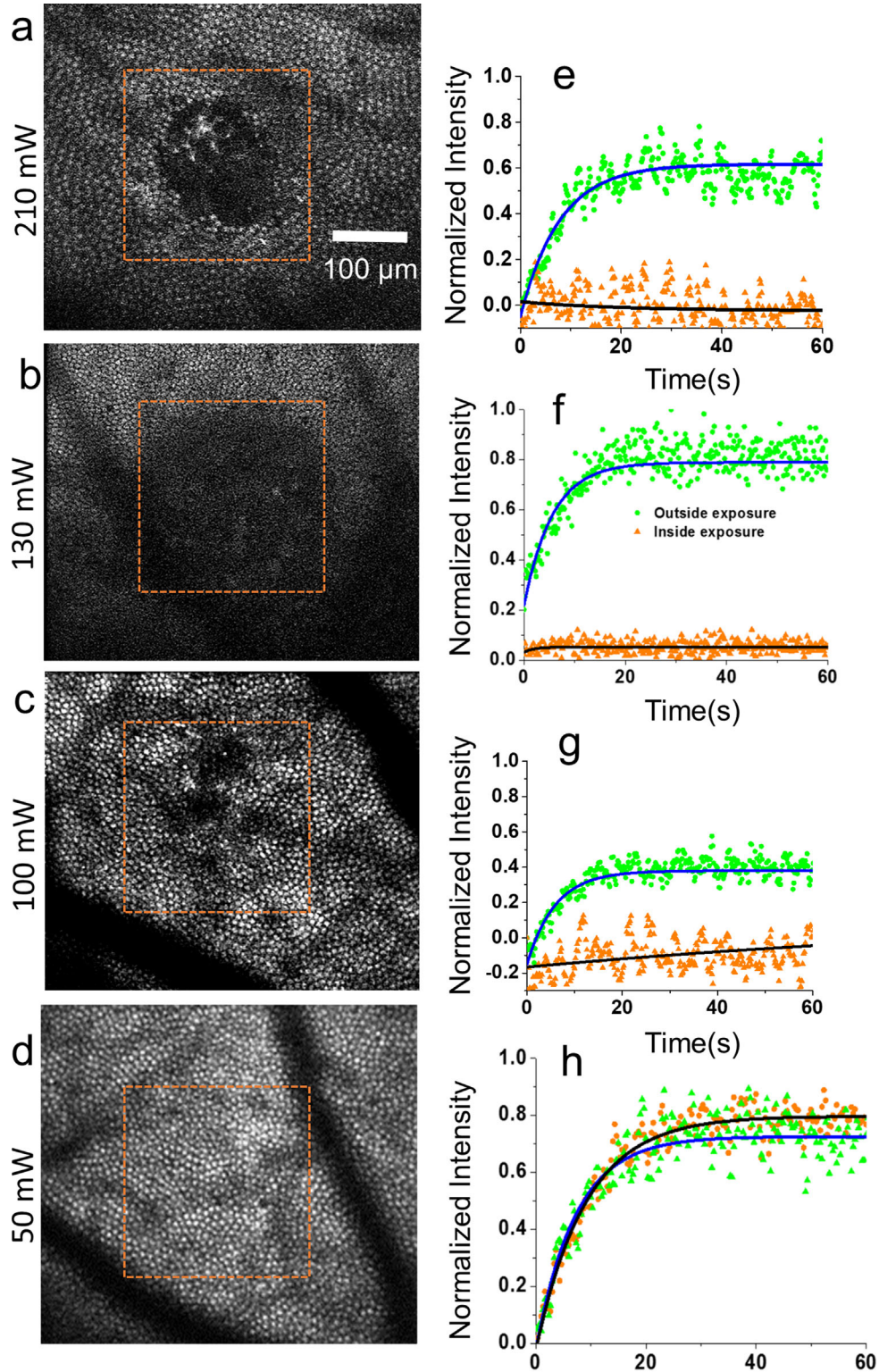


**Figure 2.** Photoreceptor structure and function within and outside lesions. (a–d) TPEF images of photoreceptors, *orange rectangle* is extent of lesion. (e–h) TPEF time profile outside and inside of exposed area for laser average powers 50, 100, 130, and 210 mW.

**Table 3.** Mean TPEF Intensity Values Inside and Outside Exposure Area

Power (mW)	Inside	Outside
210	13	45
150	29	42
130	17	74
100	25	52
80	27	50
50	49	50

the mean TPEF intensity inside and outside of the lesions for exposure powers from 50 to 210 mW. A *t*-test comparison of TPEF intensity within and without the lesion resulted in a  $t = 4.2$ , degree of freedom = 5, with the difference significant beyond the 0.05 level.

At the onset of the laser excitation, TPEF of normally functioning photoreceptors increases exponentially and after several seconds reaches a plateau, indicating that bleached photopigment is being converted to all-*trans*-retinol in the visual cycle.<sup>25</sup> Exponential fits to the TPEF of photoreceptors outside the exposed region at higher power (130 mW) yielded a fractional TPEF increase of  $0.72 \pm 0.01$ , whereas inside the exposed region TPEF was severely reduced with a TPEF increase of only  $0.37 \pm 0.01$ . The time course and fractional increase of TPEF for the lower level laser exposure (50 mW) was similar both within and surrounding the exposed region.

## Effect on RPE Cells

### Functional Assessment of RPE Tight Junctions

Fluorescein angiography was carried out to examine the effect of femtosecond laser exposure on RPE tight junctions. As shown in Figure 3a, fluorescein leakage was substantial for four lesions (120–180 mW) examined 1h post-exposure. In addition, minimal fluorescein leakage was observed at two exposure locations at power levels 80 mW and 100 mW. By 72 hours after exposure, there was no fluorescein leakage at any lesion location. This suggests a rupture of RPE cell tight junctions initially at higher laser average powers, but complete recovery after 72 hours (Fig. 3c).

### In-Vivo RPE Autofluorescence

Figures 3d to 3g show single photon autofluorescence images of the mosaic of RPE cells exposed to laser average power ranging from 80 to 180 mW. Each RPE cell nucleus is visible as a dark circle, surrounded by a diffuse bright ring, which shows the autofluorescence of the lipofuscin distributed in the cytoplasm

of the RPE cells. Retinal blood vessels appear as dark shadows overlying the RPE mosaic. In vivo AOSLO RPE autofluorescence imaging of the exposed regions 50 days after exposure revealed that at all power levels less than 100 mW there was a decrease in RPE autofluorescence in Figures 3d and 3e, but it was severely altered, and the RPE mosaic appeared highly disrupted at the higher powers as shown in Figures 3f and 3g.

## Effect on the Inner Retina

### Histologic Assessment

Stained, 3- $\mu$ m-thick sections of the lasered regions of retina show complete loss of the ONL and photoreceptor outer segments over distinct, well-defined regions (Fig. 4). The diameter of these regions appeared to correlate with the laser power used (100–120 mW), with the smallest area of missing ONL seen at 100 mW, and the largest at 120 mW. In contrast, the inner retina appears completely unaltered compared with unexposed retina.

### OCT Imaging

The axial extent of each lesion was measured from OCT B-scans taken three months after damage. When plotted as a function of average laser power (Fig 5a), the axial extent of damage increases, consistent with the histological findings denoted above and illustrated in Figure 4. In addition, we observed subtle but consistent changes in blue reflectance, blue autofluorescence, infrared reflectance and infrared autofluorescence SLO imaging after femtosecond laser exposure at all but the lowest power (50 mW) as shown in Table 2 (HRA). Figures 5c–5e show OCT images taken 12 months after exposure with average powers of 100, 150, and 180 mW, clearly illustrating the larger lesion diameter. There was no sign of inner plexiform or ganglion cell layer disorganization in the OCT images, again consistent with histologic findings above (Fig. 4). As observed in Figures 5d and 5e, a hyperreflective OCT signal was consistently observed below the RPE at all laser powers of 110 mW or greater. At powers of 100 mW or lower, no hyperreflective OCT signal was observed in Figure 5c.

### In-Vivo Vasculature Imaging of Inner Retina

Figures 6a and 6b show 790 nm AOSLO reflectance images of photoreceptors before and after exposure. Figures 6c and 6d show motion contrast images of blood flow through the deepest retinal capillaries, and Figures 6e and 6f show motion contrast images for the most superficial vessels before and after laser exposure respectively. No vasculature damage or alteration in blood flow was seen. Video images of

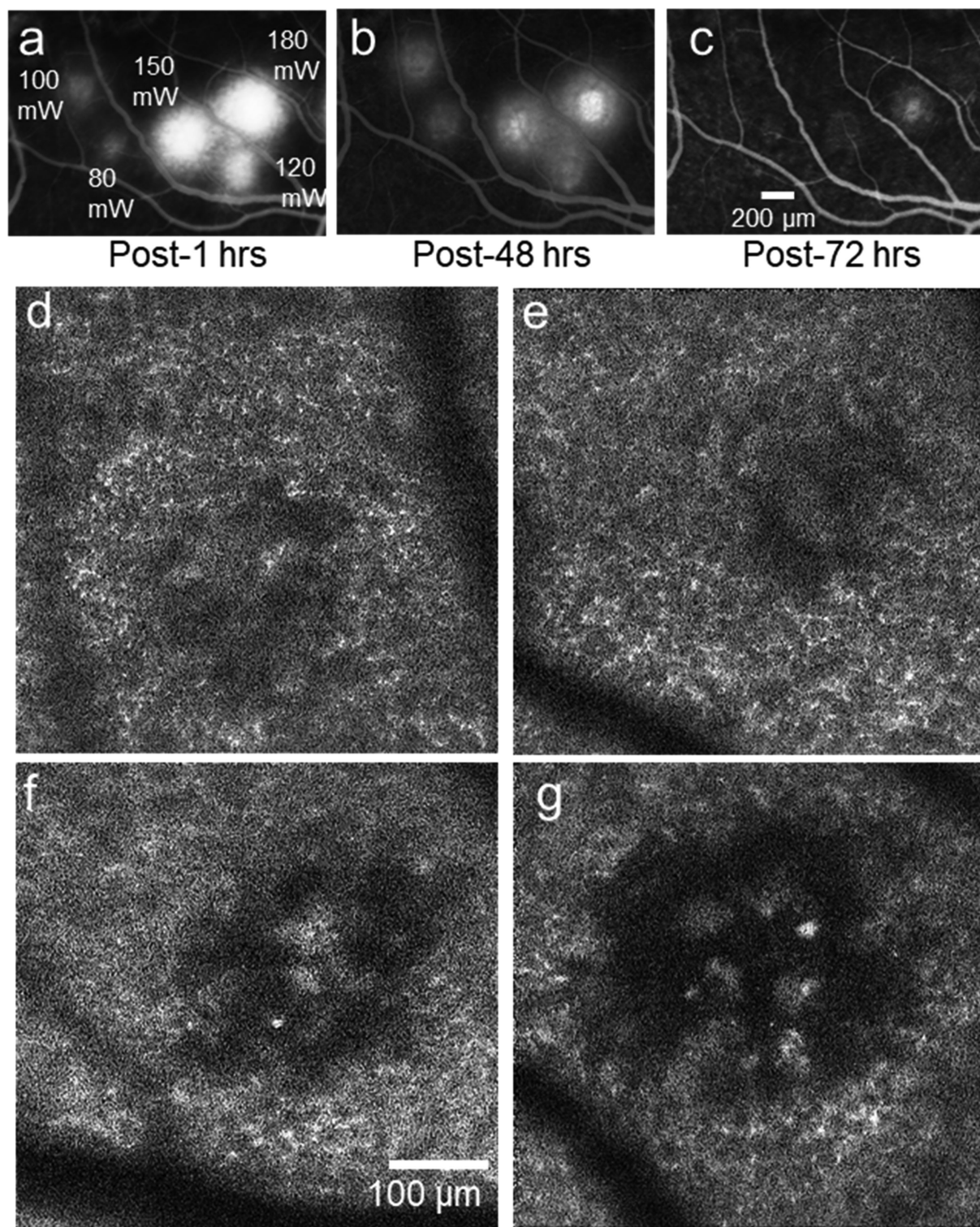


**Figure 3.** (a–c) 5.5-minute post injection fluorescein leakage shows rupture of RPE tight junctions one and 48 hours post lesion, but largely recovered by 72 hours. AOSLO autofluorescence images of the RPE mosaic at the lesion site at laser average power (d) 80 mW, (e) 100 mW, (f) 120 mW, and (g) 180 mW, respectively, for a duration of 106 ms (monkey M1).

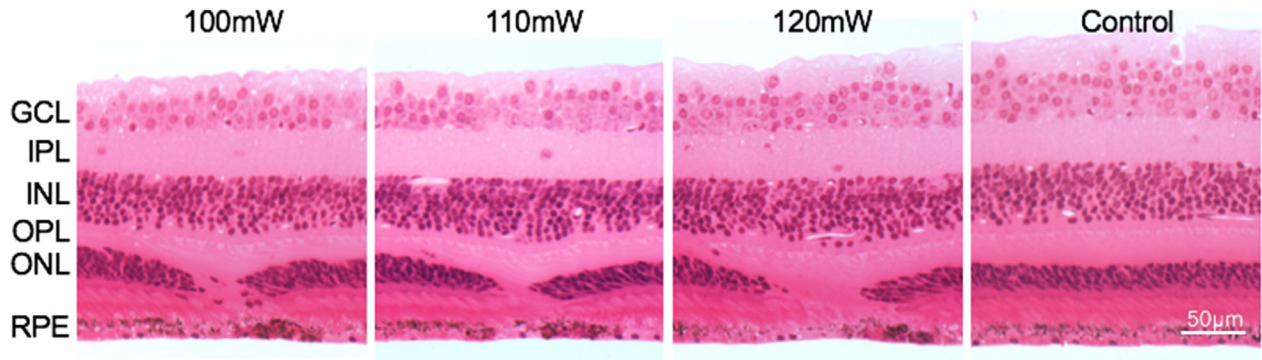


**Figure 4.** Histologic cross-sections of a monkey retina (M4) in the approximate center of laser lesions made at 100, 110, and 120 mW (106 ms duration). Note the localized loss of photoreceptors, with a complete ablation of the ONL over an increasingly larger diameter zone as laser power increased. In contrast, the inner nuclear layer (INL) and other layers of the anterior retina above the damaged zone appear structurally intact. A “control” region of unlasered retina at an eccentricity close to the 120mW ablation is included for comparison. GCL, ganglion cell layer; IPL, inner plexiform layer; INL, inner nuclear layer; OPL, outer plexiform layer; RPE, retinal pigment epithelial layer.

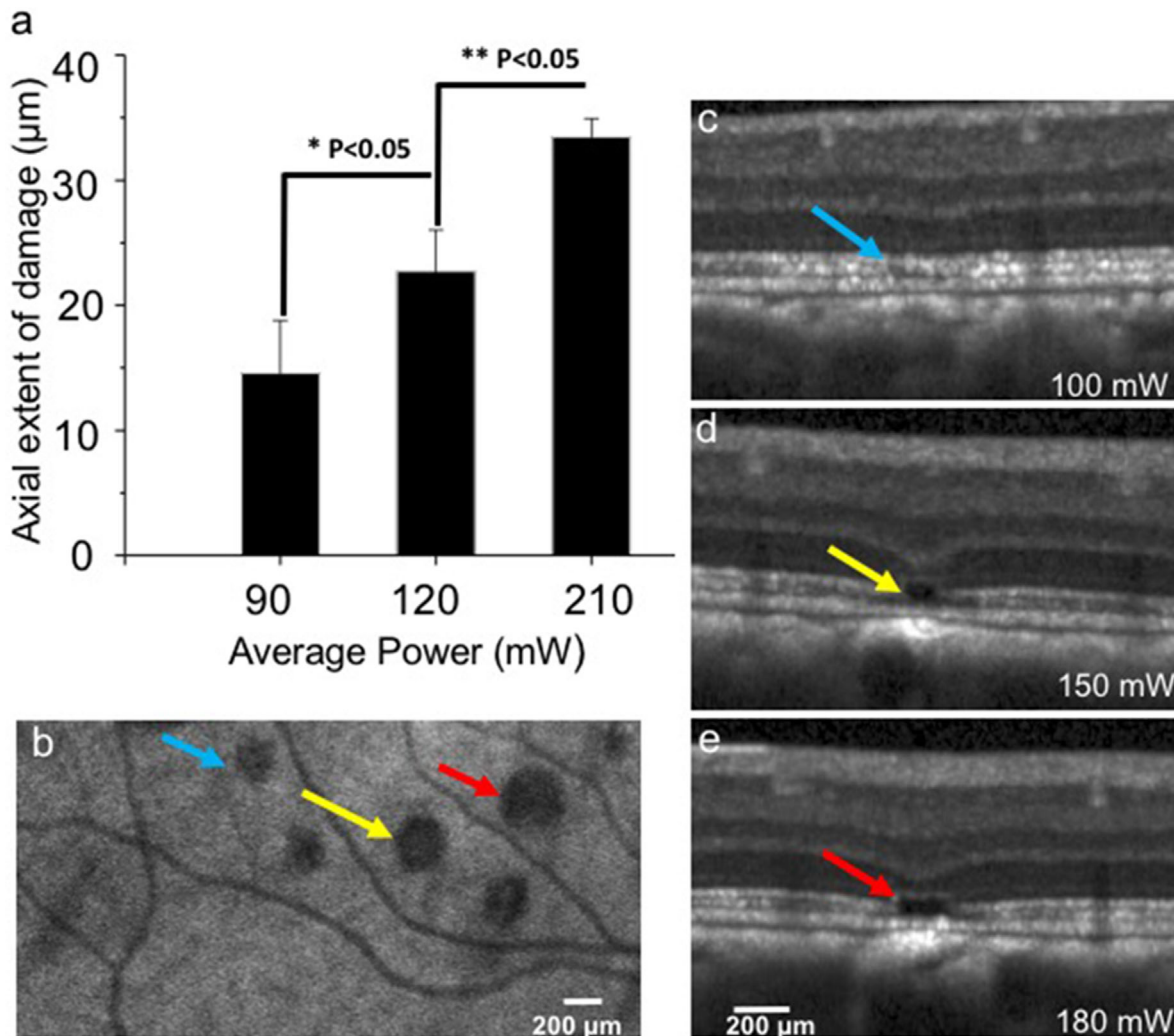


**Figure 5.** Lateral and axial visualization of lesions. (a) Measurement of axial extent of lesion from OCT-B scans (mean ± SD, one-tail Student’s *t* test). (b) Infrared autofluorescence cSLO images of lesion sites showing the enface view of lesions (100, 150, and 180 mW) marked by blue, yellow, and red arrows, respectively. (c–e) OCT B-scan images show axial localization of lesion at laser average powers marked by arrows.

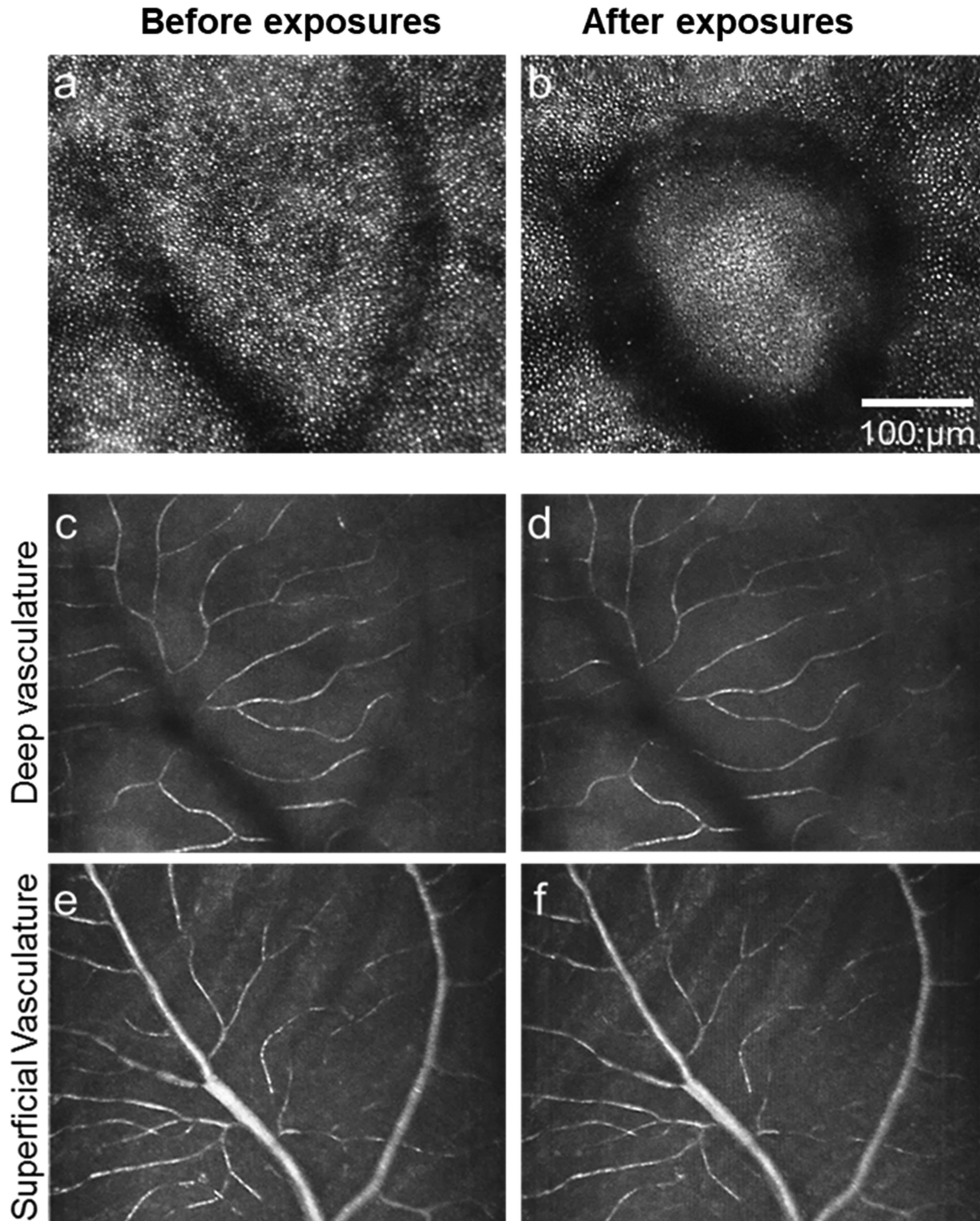


**Figure 6.** Assessment of retinal vasculature. Top panel (a, b) shows AOSLO imaging of a location before and after exposure (130 mW, 106 ms), respectively. Through focus AOSLO imaging shows no vasculature rupture. AOSLO reflectance (790 nm) motion contrast images of deep retinal vasculature before (c) and after (d) laser exposure, respectively. AOSLO reflectance (790 nm) imaging of superficial retinal vasculature before (e) and after (f) laser exposure, respectively (monkey M1).

pre-exposure and postexposure blood flow at these two locations are shown in Supplementary Movie S1 and Supplementary Movie S2.

### Response of Ganglion Cells Measured With Calcium Imaging AOSLO

In monkey M3, the calcium response of RGCs was measured in a region directly above a 150-mW laser exposure and compared to the response of RGCs from a control location. Figure 7a shows an OCT image with the location of the 150-mW lesion highlighted by the yellow box, whereas the foveal ganglion cell somas through which the laser was directed are highlighted by a blue box. These cells have displaced receptive fields that are located at the fovea center, and therefore should remain responsive to a visual stimulus if the laser-induced damage is axially localized to the outer retina. Figure 7b shows a fluorescence image from the same field of view showing the GCaMP expressing RGCs. The RGCs directly above the lesioned area are labeled green; RGCs in a control region outside of the lesioned area are labeled red. A reflectance image of the lesion within the photoreceptor layer is shown in Figure 7c. The lower left panel shows the average Fourier amplitude of the segmented cells from both the regions outside of the lesion (Fig. 7d) and directly above the lesion (Fig. 7e) to a 0.2-Hz visual stimulus. The response amplitude is the same in the two cases, indicating that the lesion is axially confined to the outer retina and has not functionally impaired the retinal ganglion cells lying directly above it.

## Discussion

This study examined a novel approach that combined femtosecond laser exposure and adaptive optics to create focally complete photoreceptor ablation in primate retina with minimal damage to other retinal neurons. Previous attempts to achieve selective damage have been unsuccessful, since laser exposure can produce diffuse retinal damage,<sup>30</sup> and substantial retinal scarring has been observed even when damage is targeted to photoreceptors.<sup>31</sup> Thus a major goal of the study was to determine whether the inner retina is functionally spared even after femtosecond laser exposures of sufficient power to cause complete loss of photoreceptors and permanent vision impairment. In this study, we tested a greater than fourfold range of laser powers and exposure durations to identify parameters that can selectively ablate the photoreceptor layer. Despite the degeneration of outer retina and persistent loss of

structure and function of photoreceptors (measured by TPEF of all-*trans*-retinol, the dominant intrinsic fluorophore found in photoreceptors) observed here, ganglion cell function was preserved at laser-treated locations. AOSLO imaging of vasculature function also showed that inner retina vascular supply was spared. The results suggest that these selective lesions could provide a useful primate model for exploring approaches to vision restoration for future application in humans. The present method, although different from a genetic model of retinal degeneration, could be beneficial in various vision restoration strategies such as electronic prostheses, optogenetics, and stem-cell therapy in animal models where genetic models are not readily available.

This primate model of eye disease does not replicate the widespread damage to most outer retinal neurons that is seen in humans and genetically appropriate models of retinal disease in transgenic mice, rats and dogs and humans.<sup>32</sup> On the other hand, relatively selective damage to outer retina may permit separation of the effects of selective photoreceptor loss from other aspects of retinal loss that are typical of human retinal disease.<sup>33</sup>

### Completeness of Photoreceptor Loss

Interpreting vision restoration is simpler in those cases with no surviving photoreceptors that could mediate “apparently restored” vision. This is a well-known complexity of some outer retinal degenerations (e.g., mouse *rd1*), where sufficient photoreceptors may survive that they can mediate fairly substantial vision.<sup>34</sup> This issue is especially problematic when measuring such functions as grating acuity, which can survive loss of most photoreceptors with little change.<sup>35</sup> Thus this study identified laser parameters that give 100% photoreceptor loss, confirmed by *in-vivo* measures of OCT and adaptive optics imaging and retinal histology.

### Short-Term and Long-Term Preservation of Inner Retina Function

Despite passage of the laser through the retinal ganglion cell layer that occurs when making exposures, the function of the RGCs is unaffected. This is a key advantage of this localized ablation approach for preclinical development of vision restoration therapies. Many methods of vision restoration depend entirely on relative preservation of ganglion cell function despite loss of outer retina, in order to enable restoration by epiretinal or subretinal optoelectronics,<sup>36,37</sup> optogenetically mediated responses of retinal ganglion cell or

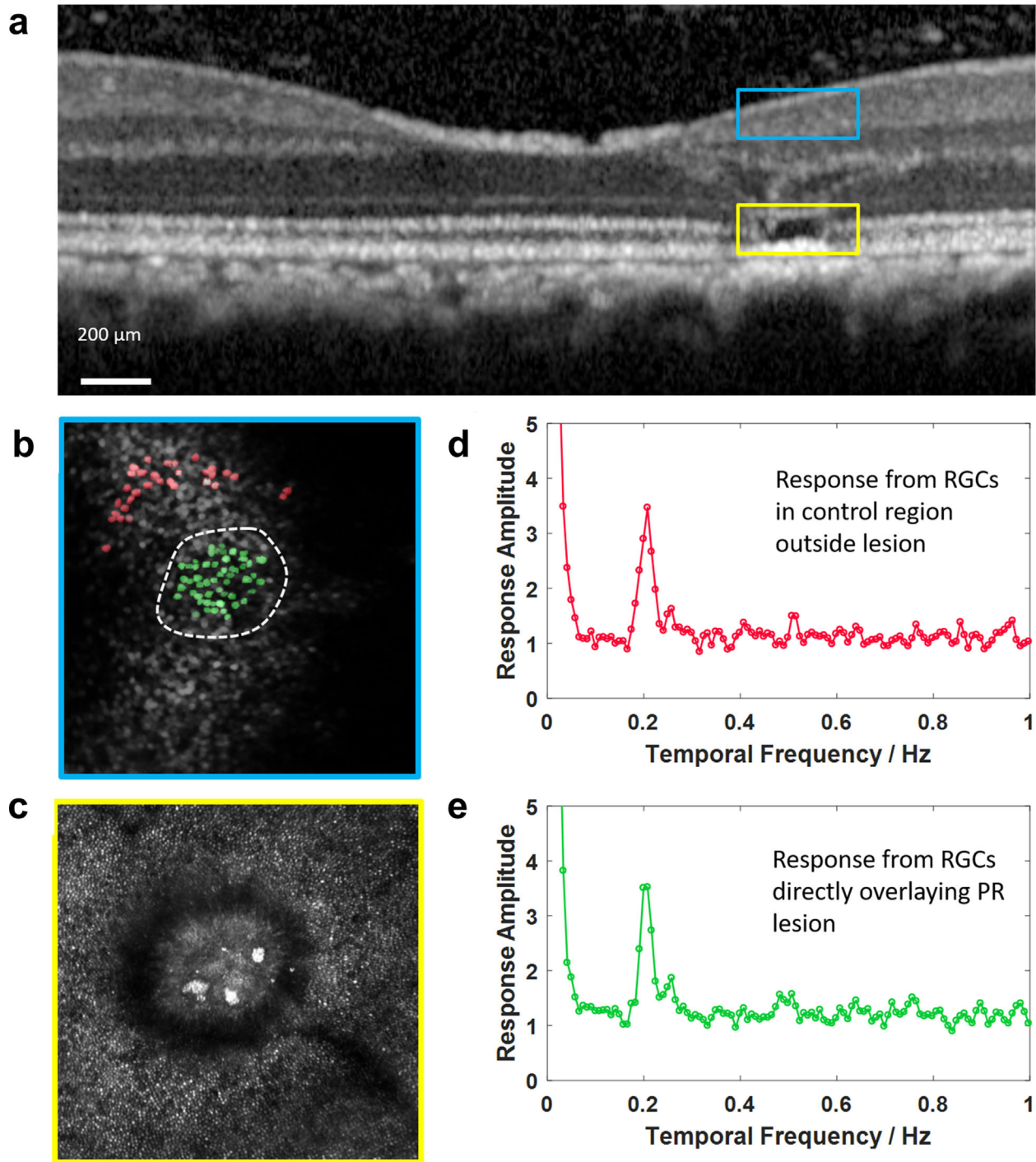


**Figure 7.** Functional measurement of ganglion cell response. *Upper panel (a)*, OCT image showing location of test lesion (150 mW, 106 ms) directly under foveal ganglion cell ring. The *yellow box* denotes the axial location of the lesion, the *blue box* shows the region of ganglion cells directly above the lesion. *Lower panel (b)* *Blue Box*: An en face AOSLO fluorescence image (525/35 nm) of the ganglion cell layer directly above the region of photoreceptor loss. Cells labeled green are right above the lesioned area (*white dashed line*). Cells labeled red are from a control region further from the lesioned area. *(c)* *Yellow box*: An en face AOSLO reflectance image of the photoreceptor layer after the ultrafast laser exposure. The *red* *(d)* and *green* *(e)* Fourier transforms show the average response of the red and green marked ganglion cells to a 0.2 Hz pan retinal visual stimulus. The laser exposure did not affect cell responsivity (monkey M3).

bipolar cells<sup>38</sup> or activation of preserved ganglion cells by photoreceptor precursors inserted into the subretinal space.<sup>39</sup>

The dependence of restoration on inner retina function is complicated by the finding of severe “remodeling” that has been observed following deprivation of photoreceptor input to inner retina.<sup>33</sup> Despite this complete loss of inner retina function is inconsistent with the success of optoelectronic restoration<sup>40</sup> showing at least partial preservation of inner retina, since the patients showing restored vision by optoelectronic devices have often been blinded by outer retina degeneration for many years. One might expect that, however good the quality of vision was at the time of treatment, the quality of preserved vision might undergo progressive decline if the inner retina continues to progressively remodel. On the other hand, it is also possible that the optoelectronically restored vision itself might slow or prevent further inner retina remodeling.

Although these questions are fundamental to the utility of vision restoration they are difficult to address. The primate model reported here should make it possible to explore such issues, since the onset of photoreceptor loss is quite abrupt and vision testing methods can be used to study long-term alteration in inner retina function. It may also be possible to ameliorate a “remodeling”-based decline in inner retina function, because a biochemical basis has been proposed for remodeling, which could make remodeling preventable if the retina is pretreated with suggested antagonists.<sup>41</sup>

## The Nature of RPE Damage

The most prominent changes observed outside the photoreceptor layer in this study were to the RPE, a monolayer of cells physically linked to photoreceptors by ciliary processes. These RPE cells support the photoreceptors in multiple ways, including renewal of photopigment in the visual cycle and physical support of the fragile photoreceptor outer segments. The health status of RPE cells in all animal models is of great importance for studying insertion of photoreceptor precursors,<sup>42,43</sup> since the survival and integration of photoreceptor replacement cells may be highly dependent on RPE for both structural support and photopigment renewal. This important role of RPE makes it urgent that we learn more about optimal animal models for studying photoreceptor replacement. The macaque preparation described here may provide an excellent model for studying photoreceptor implantation, as shown in other studies,<sup>44</sup> RPE cells rapidly recover from major insults including surgical

removal, apparently by generating a new monolayer of cells with apparently normal structure (as long as Bruch’s membrane remains intact). Thus, the present macaque model could be more favorable for the survival of photoreceptor precursors than the degenerated human retina for which this therapy is ultimately being developed. Future studies can examine this issue by separately implanting photoreceptor precursors alone, RPE precursors alone, or combined photoreceptor/RPE precursors, possibly given mechanical support by incorporation in a scaffold.<sup>45,46</sup>

## The Mechanism of Photodamage

It is likely that the photodamage observed here is due to a combination of photomechanical damage due to multiphoton absorption as a consequence of the high peak power of the ultrashort pulses<sup>47</sup> and photothermal damage due to absorbance of 730 nm light by melanin and other chromophores present in retina. Photodamage is limited primarily to the photoreceptors, but photothermal damage could be causing RPE disruption because damage might not purely photomechanical. Use of adaptive optics increases the likelihood of nonlinear interaction produced by the ultrashort pulse laser by creating a near diffraction-limited focal volume, as shown in Supplementary Figures S1a and S1b. Details of the calculation of peak laser intensity and likelihood of photomechanical damage by femtosecond laser pulse is described in [Appendix A](#).

## Experimental Advantages of the Method Described Here

A substantial limitation of the macaque model of outer retina loss described here is that it does not replicate the actual eye disease the restoration therapy is being developed to treat. Such genetically precise retinal diseases are widely available in other species, especially mouse, rat, and dog,<sup>32</sup> although both naturally occurring and transgenic models will be available in the future in primates.<sup>48,49</sup> One major benefit of the present model is that it can produce small lesions of photoreceptors at multiple retinal locations in each tested animal. The small lesions can be made smaller than the optic disc, which produces an approximately five-by-eight-degree blind spot in every eye. This blind region in each eye, as well as local visual loss of up to about 7° diameter produced by visual disease can be recognized by humans only under unusual circumstances, because of the phenomenon of cortical filling in.<sup>50</sup> Thus small lesions of the retina are probably not detectable by laboratory nonhuman primates. A second

benefit of small retinal lesions is that they permit comparison of lost vision to the function of nearby retinal locations that function normally. This is important for the adaptive optics calcium imaging method used in the present study because the method needs to adjust imaging focus with respect to the reflection from the photoreceptor layer at nearby normal retina locations. Small lesions are also important for future perceptual studies of optogenetic restoration to permit initial training of the monkey on perceptual discrimination at nearby seeing locations before moving slowly to the lesioned location. This also permits developing specific training of visual perception at locations of photoreceptor loss, which may provide a visual experience novel to the macaque. Finally, precise local lesioning of photoreceptors will provide a model to evaluate any change in visual function that results from loss of photoreceptor input. These advantages suggest that the model of retina degeneration described here may be valuable in initial development of optogenetic methods for use in human, followed by studies in nonhuman primate models of the exact outer retina disorders to be targeted in humans.

## Conclusions

These results suggest that the lesions created from femtosecond laser in conjunction with adaptive optics could provide a useful primate model for exploring restoration of visual function in nonhuman primates model. This approach, although different from a genetic model of retinal degeneration, could be beneficial in various vision restoration strategies such as electronic prostheses, optogenetics and stem-cell therapy in animal models where genetic models are not readily available.

## Acknowledgments

The authors thank Amber Walker for handling the animals and Thurma McDaniel and Sarah Mack for assistance with histology. Image acquisition and registration software was developed by Qiang Yang. Adaptive optics control software was developed by Alfredo Dubra and Kamran Ahmad and maintained by Keith Parkins. The stereotaxic cart was designed by the United States Air Force Research Laboratories and constructed with modifications by Martin Gira and Mark Dietz at the University of Rochester.

Supported by the National Institutes of Health (R01EY021166, U01EY025497 and P30EY001319) and Research to Prevent Blindness. The content is

solely the responsibility of the authors and does not necessarily represent the official views of the National Institutes of Health.

Disclosure: **K.R. Dhakal**, None; **S. Walters**, None; **J.E. McGregor**, None; **C. Schwarz**, None; **J.M. Strazzeri**, None; **E. Aboualizadeh**, None; **B. Bateman**, None; **K.R. Huxlin**, None; **J.J. Hunter**, None; **D.R. Williams**, Canon Inc. (R), P; **W.H. Merigan**, None

## References

1. Russell S, Bennett J, Wellman JA, et al. Efficacy and safety of voretigene neparvovec (AAV2-hRPE65v2) in patients with RPE65-mediated inherited retinal dystrophy: a randomised, controlled, open-label, phase 3 trial. *Lancet*. 2017;390:849–860.
2. Pearson RA, Barber AC, Rizzi M, et al. Restoration of vision after transplantation of photoreceptors. *Nature*. 2012;485:99–103.
3. MacLaren RE, Pearson RA, MacNeil A, et al. Retinal repair by transplantation of photoreceptor precursors. *Nature*. 2006;444:203–207.
4. Tochitsky I, Helft Z, Meseguer V, et al. How azobenzene photoswitches restore visual responses to the blind retina. *Neuron*. 2016;92:100–113.
5. Doroudchi MM, Greenberg KP, Liu J, et al. Virally delivered channelrhodopsin-2 safely and effectively restores visual function in multiple mouse models of blindness. *Mol Ther*. 2011;19:1220–1229.
6. Tomita H, Sugano E, Murayama N, et al. Restoration of the majority of the visual spectrum by using modified Volvox channelrhodopsin-1. *Mol Ther*. 2014;22:1434–1440.
7. Dacey DM. Parallel pathways for spectral coding in primate retina. *Annu Rev Neurosci*. 2000;23:743–775.
8. Horwitz GD. What studies of macaque monkeys have told us about human color vision. *Neuroscience*. 2015;296:110–115.
9. Harwerth RS, Smith EL. Rhesus-monkey as a model for normal vision of humans. *Am J Optom Phys Opt*. 1985;62:633–641.
10. Moshiri A, Chen R, Kim S, et al. A nonhuman primate model of inherited retinal disease. *J Clin Invest*. 2019;129:863–874.
11. Chen YY, Liu SL, Hu DP, Xing YQ, Shen Y. N-methyl- N-nitrosourea-induced retinal degeneration in mice. *Exp Eye Res*. 2014;121:102–113.
12. Yoshizawa K, Kuwata M, Kawanaka A, Uehara N, Yuri T, Tsubura A. N-methyl-N-nitrosourea-

- induced retinal degeneration in mice is independent of the p53 gene. *Mol Vis.* 2009;15:2919–2925.
13. Hara A, Niwa M, Aoki H, et al. A new model of retinal photoreceptor cell degeneration induced by a chemical hypoxia-mimicking agent, cobalt chloride. *Brain Res.* 2006;1109:192–200.
  14. Shirai H, Mandai M, Matsushita K, et al. Transplantation of human embryonic stem cell-derived retinal tissue in two primate models of retinal degeneration. *Proc Natl Acad Sci USA.* 2016;113:E81–90.
  15. Wood JPM, Shibebe O, Plunkett M, Casson RJ, Chidlow G. Retinal damage profiles and neuronal effects of laser treatment: comparison of a conventional photocoagulator and a novel 3-nanosecond pulse laser. *Invest Ophthalmol Vis Sci.* 2013;54:2305–2318.
  16. Wood EH, Leng T, Schachar IH, Karth PA. Multi-modal longitudinal evaluation of subthreshold laser lesions in human retina, including scanning laser ophthalmoscope-adaptive optics imaging. *Ophthalmic Surg Lasers Imaging Retina.* 2016;47:268–275.
  17. Sander B, Larsen M, Engler C, Moldow B, Lund-Andersen H. Diabetic macular oedema: the effect of photocoagulation on fluorescein transport across the blood-retinal barrier. *Brit J Ophthalmol.* 2002;86:1139–1142.
  18. Brancato R, Pratesi R, Leoni G, Trabucchi G, Vanni U. Histopathology of Diode and Argon-Laser Lesions in Rabbit Retina - a Comparative-Study. *Invest Ophth Vis Sci.* 1989;30:1504–1510.
  19. Yu DY, Cringle SJ, Su E, Yu PK, Humayun MS, Dorin G. Laser-induced changes in intraretinal oxygen distribution in pigmented rabbits. *Invest Ophthalmol Vis Sci.* 2005;46:988–999.
  20. Wang J, Quan Y, Dalal R, Palanker D. Comparison of continuous-wave and micropulse modulation in retinal laser therapy. *Invest Ophthalmol Vis Sci.* 2017;58:4722–4732.
  21. Levi JR, Veerappan A, Chen B, Mirkov M, Sierra R, Spiegel JH. Histologic evaluation of laser lipolysis comparing continuous wave vs pulsed lasers in an in vivo pig model. *Arch Facial Plast Surg.* 2011;13:41–50.
  22. Neev J, Da Silva LB, Feit MD, Perry MD, Rubenchik AM, Stuart BC. Ultrashort pulse lasers for hard tissue ablation. *Ieee J Sel Top Quant.* 1996;2:790–800.
  23. Han DP, Croskrey JA, Dubis AM, Schroeder B, Rha J, Carroll J. Adaptive optics and spectral-domain optical coherence tomography of human photoreceptor structure after short-duration [corrected] pascal macular grid and panretinal laser photocoagulation. *Arch Ophthalmol.* 2012;130:518–521.
  24. Sharma R, Schwarz C, Williams DR, Palczewska G, Palczewski K, Hunter JJ. In vivo two-photon fluorescence kinetics of primate rods and cones. *Invest Ophthalmol Vis Sci.* 2016;57:647–657.
  25. Walters S, Schwarz C, Sharma R, et al. Cellular-scale evaluation of induced photoreceptor degeneration in the living primate eye. *Biomed Opt Express.* 2019;10:66–82.
  26. Sharma R, Schwarz C, Hunter JJ, Palczewska G, Palczewski K, Williams DR. Formation and clearance of all-trans-retinol in rods investigated in the living primate eye with two-photon ophthalmoscopy. *Invest Ophthalmol Vis Sci.* 2017;58:604–613.
  27. Morgan JI, Dubra A, Wolfe R, Merigan WH, Williams DR. In vivo autofluorescence imaging of the human and macaque retinal pigment epithelial cell mosaic. *Invest Ophthalmol Vis Sci.* 2009;50:1350–1359.
  28. Yin L, Masella B, Dalkara D, et al. Imaging light responses of foveal ganglion cells in the living macaque eye. *J Neurosci.* 2014;34:6596–6605.
  29. Yang Q, Zhang J, Nozato K, et al. Closed-loop optical stabilization and digital image registration in adaptive optics scanning light ophthalmoscopy. *Biomed Opt Express.* 2014;5:3174–3191.
  30. Marshall J, Bird AC. A comparative histopathological study of argon and krypton laser irradiations of the human retina. *Br J Ophthalmol.* 1979;63:657–668.
  31. Strazzeri JM, Hunter JJ, Masella BD, et al. Focal damage to macaque photoreceptors produces persistent visual loss. *Exp Eye Res.* 2014;119:88–96.
  32. Baehr W, Frederick JM. Naturally occurring animal models with outer retina phenotypes. *Vision Res.* 2009;49:2636–2652.
  33. Marc RE, Jones BW, Watt CB, Strettoi E. Neural remodeling in retinal degeneration. *Prog Retin Eye Res.* 2003;22:607–655.
  34. Thyagarajan S, van Wyk M, Lehmann K, Löwel S, Feng G, Wässle H. Visual function in mice with photoreceptor degeneration and transgenic expression of channelrhodopsin 2 in ganglion cells. *J Neurosci.* 2010;30:8745–8758.
  35. Ratnam K, Carroll J, Porco TC, Duncan JL, Roorda A. Relationship between foveal cone structure and clinical measures of visual function in patients with inherited retinal degenerations. *Invest Ophthalmol Vis Sci.* 2013;54:5836–5847.
  36. Jones BW, Pfeiffer RL, Ferrell WD, Watt CB, Marmor M, Marc RE. Retinal remodeling in human retinitis pigmentosa. *Exp Eye Res.* 2016;150:149–165.
  37. Ghezzi D, Antognazza MR, Maccarone R, et al. A polymer optoelectronic interface restores light

- sensitivity in blind rat retinas. *Nat Photonics*. 2013;7:400–406.
38. Chaffiol A, Caplette R, Jaillard C, et al. A new promoter allows optogenetic vision restoration with enhanced sensitivity in macaque retina. *Mol Ther*. 2017;25:2546–2560.
  39. Mace E, Caplette R, Marre O, et al. Targeting channelrhodopsin-2 to ON-bipolar cells with vitreally administered AAV restores ON and OFF visual responses in blind mice. *Mol Ther*. 2015;23:7–16.
  40. da Cruz L, Coley BF, Dorn J, et al. The Argus II epiretinal prosthesis system allows letter and word reading and long-term function in patients with profound vision loss. *Br J Ophthalmol*. 2013;97:632–636.
  41. Telias M, Denlinger B, Helft Z, Thornton C, Beckwith-Cohen B, Kramer RH. Retinoic acid induces hyperactivity, and blocking its receptor unmasks light responses and augments vision in retinal degeneration. *Neuron*. 2019;102:574–586.e575.
  42. Phillips MJ, Wallace KA, Dickerson SJ, et al. Blood-derived human iPS cells generate optic vesicle-like structures with the capacity to form retinal laminae and develop synapses. *Invest Ophthalmol Vis Sci*. 2012;53:2007–2019.
  43. Warre-Cornish K, Barber AC, Sowden JC, Ali RR, Pearson RA. Migration, integration and maturation of photoreceptor precursors following transplantation in the mouse retina. *Stem Cells Dev*. 2014;23:941–954.
  44. Machalinska A, Kłos P, Baumert B, et al. Stem cells are mobilized from the bone marrow into the peripheral circulation in response to retinal pigment epithelium damage—a pathophysiological attempt to induce endogenous regeneration. *Curr Eye Res*. 2011;36:663–672.
  45. Gasparini SJ, Llonch S, Borscht O, Ader M. Transplantation of photoreceptors into the degenerative retina: current state and future perspectives. *Prog Retin Eye Res*. 2019;69:1–37.
  46. Lavik EB, Klassen H, Warfvinge K, Langer R, Young MJ. Fabrication of degradable polymer scaffolds to direct the integration and differentiation of retinal progenitors. *Biomaterials*. 2005;26:3187–3196.
  47. Roider J, Hillenkamp F, Flotte T, Birngruber R. Microphotocoagulation: selective effects of repetitive short laser pulses. *Proc Natl Acad Sci USA*. 1993;90:8643–8647.
  48. Moshiri A, Chen R, Kim S, et al. A nonhuman primate model of inherited retinal disease. *J Clin Invest*. 2019;129:863–874.
  49. Francis PJ, Appukuttan B, Simmons E, et al. Rhesus monkeys and humans share common susceptibility genes for age-related macular disease. *Hum Mol Genet*. 2008;17:2673–2680.
  50. Zur D, Ullman S. Filling-in of retinal scotomas. *Vision Res*. 2003;43:971–982.
  51. Roider J, Hillenkamp F, Flotte T, Birngruber R. Microphotocoagulation—selective effects of repetitive short laser-pulses. *Proc Natl Acad Sci USA*. 1993;90:8643–8647.
  52. Puliafito CA, Birngruber R, Deutsch TF, Fujimoto JG, Stern D, Zysset B. Laser-tissue interactions in the nanosecond, picosecond and femtosecond time domains. *Springer Series Opti*. 1990;62:420–427.
  53. Poudel MP. Study of self-focusing effect induced by femtosecond photodisruption on model substances. *Opt Lett*. 2009;34:337–339.
  54. Takita A, Hayasaki Y. Dynamics of femtosecond laser-induced breakdowns in water. In: *Laser Applications in Microelectronic and Optoelectronic Manufacturing VII*. 2009;7201:72010J.
  55. Vogel A, Noack J, Mittmann G, Paltauf G. Femtosecond-laser-produced low-density plasmas in transparent biological media: A tool for the creation of chemical, thermal and thermomechanical effects below the optical breakdown threshold. *Comm Biomed Appl Ultrafast Free Electron Lasers*. 2002;4633:23–37.
  56. Shen YR. Self-focusing and filaments of light: past and present. *Top Appl Phys*. 2009;114:3–19.
  57. Cain CP, Thomas RJ, Noojin GD, et al. Sub-50-fs laser retinal damage thresholds in primate eyes with group velocity dispersion, self-focusing and low-density plasmas. *Graefes Arch Clin Exp Ophthalmol*. 2005;243:101–112.
  58. Schwarz C, Sharma R, Fischer WS, et al. Safety assessment in macaques of light exposures for functional two-photon ophthalmoscopy in humans. *Biomed Opt Express*. 2016;7:5148–5169.
  59. Kennedy PK. A first-order model for computation of laser-induced breakdown thresholds in ocular and aqueous-media .1. Theory. *IEEE J Quantum Elect*. 1995;31:2241–2249.
  60. Kennedy PK, Boppart SA, Hammer DX, Rockwell BA, Noojin GD, Roach WP. A first-order model for computation of laser-induced breakdown thresholds in ocular and aqueous-media .2. Comparison to experiment. *IEEE J Quantum Elect*. 1995;31:2250–2257
  61. Vogel A, Noack J, Huttmann G, Paltauf G. Low-density Plasmas below the optical breakdown threshold—Potential hazard for multiphoton

ton microscopy, and a tool for the manipulation of intracellular events. *Multiphoton Microscopy in the Biomedical Sciences II*. 2002;4620:202–216.

## Appendix A. Theoretical Estimation of Photomechanical Damage

The high peak power associated with short or ultrashort pulses is prone to cause photomechanical damage in transparent or low absorbing tissue.<sup>51,52</sup> The nonlinear dependence of the refractive index of the material on applied electric field (irradiance) also known as the Kerr-effect can cause self-focusing of the laser beam.<sup>53</sup> High peak power of the laser pulse can also cause multiphoton ionization and thus plasma formation or dielectric breakdown if photons have sufficient energy to overcome the band-gap energy.<sup>54</sup> Plasma has absorptive properties that are different from those of ordinary gases.<sup>55</sup> Here, the critical power for self-focusing and plasma formation was calculated and compared to the estimated peak power when exposing the retina to an average power.

### (i) Laser Peak Power

Considering the constant repetition rate  $f_{\text{rep}} = 1/T$ , where T is one full period, E is the energy per pulse and  $\tau$  is the pulse width of femtosecond laser.

Peak power is defined as rate of energy per pulse

$$P_{\text{peak}} = E/\tau, \quad (\text{A1})$$

Where the average power is rate of energy over one full cycle.

$$P_{\text{avg}} = E/T \quad (\text{A2})$$

Therefore, the peak power

$$P_{\text{peak}} = \frac{P_{\text{avg}}}{f_{\text{rep}} \cdot \tau} \quad (\text{A3})$$

Considering the form factor for Gaussian beam

$$P_{\text{peak}} = 0.94x \frac{P_{\text{avg}}}{f_{\text{rep}} \cdot \tau} \quad (\text{A4})$$

Our highest average power used in this study was 210 mW, corresponding to a peak power in our study,

$$P_{\text{peak}} = 0.94x \frac{210 \text{ mW}}{80 \text{ MHz} \cdot .55 \text{ fs}} \approx 45 \text{ kW} \quad (\text{A5})$$

### (ii) Self-focusing

Self-focusing occurs if the laser peak power approaches the critical power,<sup>56</sup>

$$P_{\text{cr,sf}} = \frac{0.148x\lambda^2}{n_1 \cdot n_2} \approx 1.34 \text{ MW} \gg P_{\text{peak}} \quad (\text{A6})$$

Where  $\lambda$  is the wavelength of light used (730 nm) and the linear and nonlinear refractive indices for vitreous

humor are  $n_1 = 1.336$  and  $n_2 = 1.4 \times 10^{-13} \text{ esu}$  respectively.

Therefore, possible damage induced by self-focusing of femtosecond laser in our study is completely neglected.

### (iii) Plasma formation

The irradiance threshold for plasma formation in the femtosecond laser pulse regime in ocular media is calculated following the example of Cain et al.<sup>57</sup> and employing the AOSLO scanner failure case by Schwarz et al.<sup>58</sup> with consideration of first order model of Kennedy with special attention to Kennedy sections IV D and V F.<sup>59,60</sup> For the ultrashort pulse regime, this model is based on the theory of multiphoton ionization. The threshold intensity for the plasma-mediated breakdown is calculated by

$$I_{\text{cr}} = \frac{(Q_{\text{cr}})^{\frac{1}{K}} * (A \cdot \tau \cdot 0.5)^{-K}}{B} \approx 10^{13} \text{ W/cm}^2 \quad (\text{A7})$$

with  $Q_{\text{cr}}$  being the critical free electron density ( $\sim 10^{18} \text{ cm}^{-3}$ ) and K is the number of photons required to ionize the medium (considering simple aqueous medium water having band gap energy ( $\Delta$ ) = 6.5 eV of the medium and  $\omega = 2.58 \times 10^{15} \text{ Hz}$  is the frequency of the laser at wavelength ( $\lambda$ ) = 730 nm.

$$K = \left(1 + \frac{\Delta}{\hbar \cdot \omega}\right) = 4 \quad (\text{A8})$$

A and B are characteristic parameters of the medium and are defined by

$$A = \left(\frac{2}{9 \cdot \pi}\right) \cdot \omega \cdot \left(\frac{m' \cdot \omega}{\hbar}\right)^{\frac{3}{2}} \cdot e^{2K} \cdot \phi(z) \cdot \left(\frac{1}{16}\right)^K \quad (\text{A9})$$

And

$$B = \frac{q^2}{m' \cdot \Delta \cdot \omega^2 \cdot c \cdot \epsilon_0 \cdot n_0} \quad (\text{A10})$$

$\omega$ , K and  $\Delta$  are the same as above, and  $\epsilon_0 = 8.85 \times 10^{-12} \text{ C/Vm}$  is the permittivity of the free space  $n_0 = 1.336$  the index of refraction of the medium at frequency  $\omega$ ,  $m' = 4.55 \times 10^{-31} \text{ kg}$  the exciton reduced mass,  $\hbar = 6.58 \times 10^{-16} \text{ eVs}$  the reduced Planck constant,  $q = 1.6 \cdot 10^{-19} \text{ C}$  the electron charge, and  $\Phi(z) = e^{-z^2} \sum_{k=0}^n \frac{z^{2k+1}}{k! \cdot (2k+1)}$  represents Dawson's integral with  $z = \sqrt{2K - \frac{2 \cdot \Delta}{\hbar \cdot \omega}}$ .

The low-density plasma formation model in aqueous media previously used by Vogel et al.<sup>61</sup> and followed by Schwarz et al.,<sup>58</sup> showed that possibility of low-density plasma formation if the laser peak intensity reaches to a particular threshold, calculated mathematically,  $I_{\text{cr}} \approx 10^{13} \text{ W/cm}^2$ . Considering diffraction limited focal spot size  $\sim 2.49 \mu\text{m}^2$  of scanning

laser beam used in this study and using peak power of the femtosecond laser used in this study as calculated in prior section (45 kW), the peak laser intensity in our study is ( $I_{\text{peak}}$ ) is  $0.18 \times 10^{13}$  W/cm<sup>2</sup>, which is comparable to the peak threshold intensity of optical breakdown ( $I_{\text{cr}} = 10^{13}$  W/cm<sup>2</sup>). Therefore, we believe the ablation of photoreceptors by the femtosecond laser reflected a photomechanical effect. However due to the presence of highly absorbent chromophores such as melanin in the retina, damage caused by a photothermal mechanism cannot be ruled out.

## Supplementary Material

Supplementary Movie S1. Adaptive optics movie of blood flow in superficial retinal vasculature before the lesion (left) and after the lesion (right). No change is visible in the superficial vasculature.

Supplementary Movie S2. Adaptive optics movie of blood flow in deep retinal vasculature before the lesion (left) and after the lesion (right). The lesion is visible in the after-lesion video.